



Cite this: *Phys. Chem. Chem. Phys.*,  
2023, 25, 26797

# Adsorption of HCN on cosmic silicates: a periodic quantum mechanical study†

Niccolò Bancone,<sup>ab</sup> Stefano Pantaleone,<sup>id a</sup> Piero Ugliengo,<sup>id a</sup> Albert Rimola<sup>id \*b</sup>  
and Marta Corno<sup>id \*a</sup>

Hydrogen cyanide (HCN) represents a small but widely distributed fraction of the interstellar molecules, and it has been observed in all the environments characterizing the formation of a new planetary system. HCN can polymerize to form biomolecules, including adenine ( $\text{H}_5\text{C}_5\text{N}_5$ ), and it has drawn attention as a possible precursor of several building blocks of life due to the presence of its polymerization products in meteorites, comets and other asteroidal bodies. To elucidate the potential catalytic role that cosmic silicates have played in these processes, we have investigated, at DFT-PBE level inclusive of a *a posteriori* dispersion correction, the energetic and spectroscopic features of the adsorption of HCN molecules on the most relevant crystalline surfaces of the mineral forsterite ( $\text{Mg}_2\text{SiO}_4$ ), a common silicate constituent of the interstellar core grains and planetary rocky bodies. The results reveal that HCN adsorbs both in molecular and dissociative ways, within a wide range of adsorption energies ( $-29.4$  to  $-466.4$  kJ mol<sup>-1</sup>). Thermodynamic and kinetic results show that dissociative adsorption is dominant already at low temperatures, a fact particularly relevant at the protoplanetary conditions (*i.e.*, the latest stages in the star system formation process). The simulated spectroscopic features of the studied adducts show a wide range of different degrees of perturbation of C–H and C≡N bonds. This finding agrees with previous experimental works, and our results confirm that a complex chemistry is observed when this astrochemically-relevant molecule interacts with  $\text{Mg}_2\text{SiO}_4$ , which may be associated with a considerable potential reactivity towards the formation of relevant prebiotic compounds.

Received 30th March 2023,  
Accepted 22nd September 2023

DOI: 10.1039/d3cp01459b

rsc.li/pccp

## Introduction

HCN has been identified in many different astrophysical environments, including protostellar hot cores/corinos,<sup>1–4</sup> protoplanetary disks,<sup>5–8</sup> comets,<sup>9,10</sup> carbonaceous chondrites,<sup>11</sup> planetary atmospheres,<sup>12–14</sup> and diffuse and dense clouds.<sup>15,16</sup> Its ability to polymerize is known since the 60's of the last century<sup>17</sup> and its products, including adenine ( $\text{H}_5\text{C}_5\text{N}_5$ ), have been identified in meteorite fragments.<sup>18</sup> HCN polymers are thought to contribute to the dark/brown color observed on the exterior of comets Halley and P/Stephan–Oterma and the observed 2.2 and 4.4 μm bands have been assigned to C≡N stretching modes.<sup>19,20</sup> The same hypothesis was also proposed for the absorption lines detected on the saturn's satellite Iapetus, the rings of uranus and some asteroids of the solar system.<sup>20</sup> In addition, some assumptions

postulate the presence of HCN polymers on titan, saturn and jupiter.<sup>21,22</sup> These premises led to the study of HCN reactivity under different conditions with the aim of identifying plausible pathways for its polymerization in interstellar and prebiotic conditions.<sup>17,23–29</sup> Possible HCN-derived prebiotic compounds are not observed in pristine and cold interstellar regions such as giant molecular clouds (GMCs) where temperatures are around 10 K.<sup>30</sup> Instead, they are observed in rather more evolved environments such as those listed above, where the conditions are less inert due to higher temperatures, reaching 150–300 K, and to a higher exposition to radiative energy inputs.<sup>18–22</sup> The presence of HCN and its prebiotic derivatives on larger celestial bodies may then be ascribable to catalytic processes taking place during later stages in planetary system formations (*e.g.*, in protoplanetary disks or on planetesimals) or on formed celestial bodies like asteroids, comets, meteorites, planets and satellites.<sup>18–22</sup>

Indeed, it has been demonstrated that gas-phase pathways are unfavoured due to high energetic barriers hindering the reaction already at its first steps, thus making it unfeasible in GMCs, where temperatures are in the order of 10 K and external energy inputs are missing.<sup>30</sup> In fact, a number of studies report that the key step for triggering the polymerization of HCN to

<sup>a</sup> Dipartimento di Chimica and NIS – Nanostructured Interfaces and Surfaces – Centre, Università degli Studi di Torino, via P. Giuria 7, 10125, Torino, Italy. E-mail: marta.corno@unito.it; Tel: +39-0116702439

<sup>b</sup> Departament de Química, Universitat Autònoma de Barcelona, 08193 Bellaterra, Spain. E-mail: albert.rimola@uab.cat; Tel: +34-935812164

† Electronic supplementary information (ESI) available. See DOI: <https://doi.org/10.1039/d3cp01459b>



adenine and nucleobases is the deprotonation of one molecule to form the nucleophilic  $\text{CN}^-$ .<sup>17,27,29</sup> Studies in the condensed phase, indeed, show that the polymerization is more favoured in basic water solutions and at solid catalytic surfaces, where basic catalysts facilitate proton transfer mechanisms.<sup>17,29,31,32</sup>

In this regard, cosmic silicates (ubiquitously present in different astrophysical environments) can be possible candidates as solid-state catalysts for the HCN polymerization. This is due to the basic behaviour of exposed  $\text{O}^{2-}$  anions,<sup>33</sup> which are expected to deprotonate adsorbed HCN molecules and provide the reactive  $\text{CN}^-$ . These minerals represent a fundamental fraction of the mineral phase of solid astronomical bodies such as dust grains,<sup>34</sup> meteorites,<sup>35</sup> cometary grains,<sup>36</sup> and rocky planets, and have been considered as solid-state matter relevant in the synthesis of cosmic molecules. The study from an atomistic point of view can provide fundamental insights on their physico-chemical features, and on the interaction and reactivity with gas-phase molecules. In that respect, quantum mechanical simulations are a powerful tool to investigate olivines (one of the most abundant families of cosmic silicates),<sup>37–41</sup> allowing to reproduce harsh environments, too. Indeed, Mg-pure olivines (*i.e.*,  $\text{Mg}_2\text{SiO}_4$ , forsterite) have been adopted as model materials in both experimental and theoretical studies, focusing, in particular, on the interaction of molecules of astronomical and prebiotic interest with amorphous and crystalline  $\text{Mg}_2\text{SiO}_4$  surfaces.<sup>33,42–62</sup>

A very recent work by Santalucia *et al.* reported the results of HCN adsorption and reactivity on crystalline  $\text{Mg}_2\text{SiO}_4$  surfaces.<sup>31</sup> The authors characterized the HCN/surface interactions and the products that result from the HCN polymerization on a laboratory scale by means of IR spectroscopy and ESI(-)/HRMS, in a first attempt of exploring the interaction of HCN with  $\text{Mg}_2\text{SiO}_4$ .

To the best of our knowledge, an *ab initio* study on this topic is still lacking. Because of that, in the present work, the interaction of HCN molecules on  $\text{Mg}_2\text{SiO}_4$  forsterite surfaces has been explored by means of density functional theory (DFT) simulations. Although the amorphous phase is dominant in many cosmic rocky bodies,<sup>63</sup> modelling the adsorption of HCN on different exposed crystalline surfaces of forsterite (*i.e.*, six faces at 0 K<sup>40</sup>), surely provides relevant insights on the intrinsic adsorption properties derived from HCN/ $\text{Mg}_2\text{SiO}_4$  interactions. The aim of this work is, thus, to propose a reliable theoretical background on the adsorption of HCN molecules on cosmic silicate surface models to elucidate the role of HCN as a prebiotic precursor and to investigate how cosmic silicates could have participated in reactions of prebiotic interest.

## Computational details

All calculations were performed with the CRYSTAL17 code,<sup>64</sup> which implements Hartree–Fock and DFT methods for periodic systems by adopting localized Gaussian Type Orbitals (GTOs). The PBE Hamiltonian<sup>65</sup> was adopted for geometry optimization and frequency calculations of all the structures. To take into

account dispersive forces, all calculations include the Grimme's empirical dispersion  $\text{D2}^{66}$  in its revised version  $\text{D}^*(N)$ ,<sup>67,68</sup> specifically customized for  $\text{Mg}^{2+}$  cations. H, C and N atoms were described with the Ahlrichs-VTZ<sup>69</sup> basis sets augmented with polarization functions whilst for forsterite atoms the smaller basis set proposed by Bruno *et al.* was adopted,<sup>40</sup> that is, 8-511G\* for Mg, 8-6311G\* for Si, and 8-411G\* for O. The exponents (in  $\text{Bohr}^{-2}$ ) of the most diffuse sp shells are 0.68 and 0.22 (Mg), 0.32 and 0.13 (Si), and 0.59 and 0.25 (O). The exponents of the d shells are 0.5 (Mg), 0.6 (Si), and 0.5 (O) (the full basis sets are available in the ESI†). The accuracy in the evaluation of the Coulomb integrals were controlled by adopting the default threshold parameters in CRYSTAL17. The default DFT grid was adopted to ensure a satisfactory accuracy in the numerical integrated electron charge density, in accordance with Bruno *et al.*<sup>40</sup> The number of  $k$  points to sample the Brillouin zone was set to 5 for all the calculations, with the only exception of the adduct of HCN on the (010) surface, where a  $2 \times 2$  supercell model was adopted and for which the number of  $k$  points was lowered to 4. Geometry optimizations were performed by adopting the Broyden–Fletcher–Goldfarb–Shanno (BFGS) algorithm.<sup>70–73</sup> The Bruno *et al.* bulk structure<sup>40</sup> was used as initial guess and both the atomic positions and the cell parameters were optimized at PBE- $\text{D}^*(N)$  level. Slabs and HCN adducts were optimized by keeping the cell parameters fixed at the bulk optimized values. When possible, symmetry was exploited to speed up the calculation. The relative stability of each surface was evaluated by computing its surface energy ( $E_s$ ) as:

$$E_s = \frac{E_{\text{slab}} - 4E_{\text{bulk}}}{2A}$$

where  $E_{\text{slab}}$  and  $E_{\text{bulk}}$  are the unit cell absolute energies of the slab and the bulk, respectively. The factor 4 considers the stoichiometric ratio 4:1 between the slabs and the bulk. For a more detailed discussion on the computation of surface energies, the reader can refer to ref. 74 For each optimized HCN/surface adduct, the adsorption energy ( $\Delta E_{\text{ads}}$ ) of the adsorbed molecules was computed as:

$$\Delta E_{\text{ads}} = E_{\text{add}} - (E_{\text{mol}} + E_{\text{slab}})$$

with  $E_{\text{add}}$ ,  $E_{\text{mol}}$  and  $E_{\text{slab}}$  being the absolute potential energies of the adduct, the isolated molecule and the bare slab, respectively. Each  $\Delta E_{\text{ads}}$  includes the correction for the dispersion through the  $\text{D}^*(N)$  term and the basis set superposition error (BSSE)<sup>75,76</sup> correction, which was performed with the “Counterpoise” method (CP).<sup>77</sup> The adsorption enthalpy at 0 K was computed by correcting the  $\Delta E_{\text{ads}}$  for the zero-point energy (ZPE) coming from the harmonic approximation in the frequency calculation:

$$\Delta H_{\text{ads}}(0) = \Delta E_{\text{ads}} + \Delta \text{ZPE}$$

where the pV and the thermal factors are neglected due to the physico-chemical conditions of a MC.<sup>78</sup>

To facilitate comparison with the experiments, all the computed  $\text{C}\equiv\text{N}$  and  $\text{C-H}$  stretching frequencies were corrected for a scaling factor  $s$  to partially recover the systematic error



associated with the PBE- $D^*(N)$  method.  $s$  was obtained as the ratio between the experimental<sup>79</sup> and the computed frequency of an isolated HCN molecule, that is:

$$s_{\text{CN}} = \frac{\bar{\nu}_{\text{exp}}(\text{CN})}{\bar{\nu}_{\text{theo}}(\text{CN})} = \frac{2097 \text{ cm}^{-1}}{2127 \text{ cm}^{-1}} = 0.9859$$

$$s_{\text{CH}} = \frac{\bar{\nu}_{\text{exp}}(\text{CH})}{\bar{\nu}_{\text{theo}}(\text{CH})} = \frac{3311 \text{ cm}^{-1}}{3370 \text{ cm}^{-1}} = 0.9825$$

The energy barriers for the dissociation of an adsorbed HCN molecule were computed by localizing the transition states (TSs) related to the proton transfer from the C atom of HCN to the closest O atom of the surface silicate. The distinguished reaction coordinate (DRC)<sup>80</sup> was adopted to localize the TSs. Activation and reaction enthalpies were computed by applying the zero-point and the thermal corrections to the potential energy variations:

$$\Delta H = \Delta E + \Delta \text{ZPE} + \Delta E_{\text{T}}$$

An in-house code developed in our group based on the Rice-Ramsperger-Kassel-Marcus (RRKM)<sup>81–84</sup> scheme (a microcanonical version of the Eyring transition state theory) was used to derive unimolecular rate constants and half-life times for the dissociation reactions. For a reaction step with an energy barrier  $E_0$ , the microcanonical rate constant  $k(E)$  at a given total energy  $E$  (with  $E > E_0$ ) is given by

$$k(E) = \frac{N^{\ddagger}(E - E_0)}{h\rho(E)} = \frac{\int_{E_0}^{E-E_0} T(\xi^{\ddagger}) \rho^{\ddagger}(E - E_0 - \xi^{\ddagger}) d\xi^{\ddagger}}{h\rho(E)}$$

where  $N^{\ddagger}(E - E_0)$  is the sum of states for the TS (where the integration range expands to energies below the barrier and not just above it),  $\rho(E)$  is the density of states of reactants (*i.e.*, the number of states per unit of energy, in quantum mechanics the degeneracy  $g(E)$ ), and  $h$  the Planck constant. The sum of states over the translational energy of the reaction coordinate  $\xi^{\ddagger}$ . Tunneling effects are included by introducing the transmission probability  $T(\xi^{\ddagger})$  inside the integral. In a final step, microcanonical  $k(E)$  can be converted into canonical  $k(T)$  by populating the energy levels according to the Boltzmann distribution,  $P(E)$ :

$$k(T) = \int_{E_0}^{\infty} k(E) \times P(E) dE = \int_{E_0}^{\infty} k(E) \times \frac{g(E) \exp(-E/k_{\text{B}}T)}{Q(T)} dE$$

for the calculation of the transmission probability  $T(\xi^{\ddagger})$ , the asymmetric Eckart potential has been used:<sup>85,86</sup>

$$T(\xi^{\ddagger}) = \frac{\cosh(a+b) - \cosh(a-b)}{\cosh(a+b) + \cosh(\sqrt{4\alpha_1\alpha_2 - \pi^2})}$$

with  $a = 2(\alpha_1\xi)^{1/2}(\alpha_1^{-1/2} + \alpha_2^{-1/2})^{-1}$ ,  $b = 2[(\xi - 1)\alpha_1 + \alpha_2]^{1/2}(\alpha_1^{-1/2} + \alpha_2^{-1/2})^{-1}$ ,  $\alpha_1 = 2\pi V_1/h\nu^{\ddagger}$ ,  $\alpha_2 = 2\pi V_2/h\nu^{\ddagger}$ ,  $\xi = E/V_1$ ,  $V_1$  being the barrier from TS to reactants,  $V_2$  the barrier from TS to products and  $\nu^{\ddagger}$  the absolute value of the frequency associated with the TS. For the cases with  $\alpha_1 \gg 1$ , such as the (010) A, (120) B, and (101) B, the symmetrical Eckart's approach was employed. Finally, we highlight that the RRKM was developed for

gas-phase processes. To adapt this theory to solid state processes only the vibrational degrees of freedom of all the species were taken into account, thus leaving aside the translational and rotational ones, since they are to be disregarded in solid state systems. Results are, in the end, equivalent to rate constants obtained with the Eyring's transition state theory accounting for only vibrational partition functions.

## Results and discussion

### Modelling of $\text{Mg}_2\text{SiO}_4$ surfaces and theoretical characterization

Forsterite ( $\text{Mg}_2\text{SiO}_4$ ) is the Mg end-member of olivines and its bulky structure presents an orthorhombic lattice ( $a \neq b \neq c$ ,  $\alpha = \beta = \gamma = 90.0^\circ$ ). It belongs to the *Pbnm* space group, although sometimes it is reported as *Pnma* space group; the only difference consists in the reference assigned to the basis vectors of the lattice, namely, in *Pbnm* the lattice parameters are  $|\mathbf{a}| = x$ ,  $|\mathbf{b}| = y$ ,  $|\mathbf{c}| = z$ , while according to the *Pnma* convention they are  $|\mathbf{a}| = z$ ,  $|\mathbf{b}| = x$ ,  $|\mathbf{c}| = y$ . For our scope, this choice has no implications, and we consider the *Pbnm* space group.

The bulk structure presents a distorted hexagonally close-packed array of  $\text{O}^{2-}$  anions.  $\text{Si}^{4+}$  cations occupy one-eighth of the available tetrahedral interstices ( $\text{SiO}_4$  units) while  $\text{Mg}^{2+}$  cations occupy one-half of the octahedral sites ( $\text{MgO}_6$  units), resulting in the displacement of  $\text{O}^{2-}$  anions and a variation of the Mg–O distance, about 2.05–2.21 Å.<sup>87,88</sup> The octahedral sites accommodating  $\text{Mg}^{2+}$  cations are usually referred to as M1 and M2 sites, M1 being more distorted and compact than M2, and forming edge-sharing chains of  $\text{Mg}^{2+}$  cations along the  $c$  axis (see Fig. 1).

In this work, both atomic positions and cell parameters of the forsterite bulk have been optimized at the PBE- $D^*(N)$  level and compared with the values calculated by Bruno *et al.* at the B3LYP level. The results are reported in Table 1, together with a comparison with the experimental data of Bostrom.<sup>89</sup> In a previous work by De la Pierre *et al.*<sup>90</sup> it was reported that the PBE functional overestimates the structural parameters of forsterite, even more than the B3LYP. The PBE- $D^*(N)$ , instead, describes the  $b$  and  $c$  parameters better than the

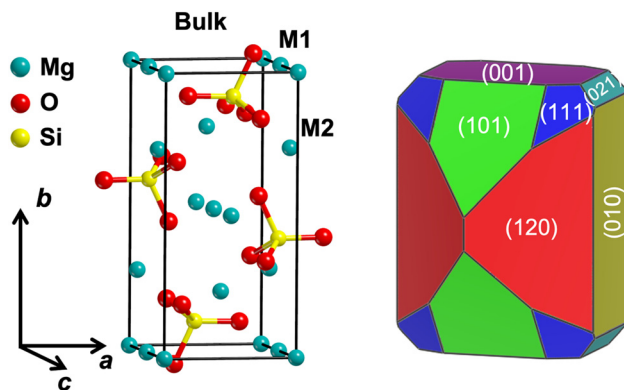


Fig. 1 Left: Forsterite bulk unit cell (cell borders are in black). Right: Wulff's construction of a forsterite nanocrystal using the computed  $E_s$  values of this work at PBE- $D^*(N)$  level.



**Table 1** Experimental and computed lattice parameters (Å) and cell volume (Å<sup>3</sup>) for forsterite bulk. Percentage variations with respect to experimental values are reported in parentheses

Parameter	Experimental <sup>89</sup>	B3LYP <sup>40</sup> (%Δ)	PBE- <i>D</i> *( <i>N</i> ) (%Δ)
<i>a</i>	4.7490	4.7892 (0.8)	4.8011 (1.1)
<i>b</i>	10.1985	10.2539 (0.5)	10.2117 (0.1)
<i>c</i>	5.9792	6.0092 (0.5)	6.0079 (0.5)
<i>V</i>	289.5887	295.0997 (1.9)	294.5534 (1.7)

dispersion-uncorrected B3LYP ones, resulting in a cell volume closer to the experimental result. This is due to the contribution of the *D*\*(*N*) correction, stabilizing compact structures.

From the optimized Mg<sub>2</sub>SiO<sub>4</sub> bulk structure, seven periodic 2D slabs of Miller indices (010), (120), (101), (001), (111), (021) and (110) were cut out (shown in Fig. 2) from the optimized bulk structure. All the considered slabs exhibit zero dipole moment across the non-periodic dimension (*z*)<sup>91</sup> also keeping the SiO<sub>4</sub> units intact. The geometry optimization of the 2D slabs was performed by keeping the cell parameters fixed at the bulk values to enforce the rigidity of the real material. The seven slabs have been characterized by computing their surface energy (*E*<sub>s</sub>) and morphological relevant index (MRI, expressed as the percentage ratio between the unit area of a single surface and the total area of the crystal). The equilibrium shape at 0 K of a forsterite nano-crystal was obtained by applying the Wulff's theorem<sup>92</sup> (see Table 2 and Fig. 1). Our *E*<sub>s</sub> values computed at PBE-*D*\*(*N*) are all lower than those computed by Zamirri *et al.* at B3LYP-*D*\*,<sup>53</sup> with an average percentage deviation of −7.3%. This is likely due to the different scheme we used for the dispersion correction. In particular, the *D*\*(*N*) scheme adopts smaller *C*<sub>6</sub> coefficients for Mg with respect to the *D*\* (see ref. 66–68 for more details), the latter determining an over-stabilization of the bulk and, thus, higher *E*<sub>s</sub> values. Despite this, the relative *E*<sub>s</sub> stability order is the same when computed with the two methods, that is: (010) < (120) < (101) < (001) < (111) < (021) < (110). The PBE-*D*\*(*N*) MRI values do not appreciably deviate from the B3LYP-*D*\* ones and the overall crystal shape is very similar. It results that the (120) face, despite being energetically less stable than the (010), is the most extended facet. It is worth mentioning that the (110) face does not appear in the Wulff's structure at any level of theory, and, for this reason, it is not considered in this work.

Interestingly, and as already pointed out by Zamirri *et al.*, more compact and regular surfaces (such as the (010) and the (001) ones) possess smaller surface areas, and, accordingly, a minor number of Mg<sup>2+</sup> sites available for adsorption. In contrast, the most irregular surfaces (such as the (120), (111) and (101) ones) show a larger number of available adsorption sites. The large *E*<sub>s</sub> value shown by the (021) surface is probably due to the highly uncoordinated Mg<sup>2+</sup> cation. King *et al.*<sup>49</sup> reported that the strength of the interaction of water molecules with forsterite is highly influenced by the degree of coordination of the available adsorption sites. According to that, it is then reasonable to expect stronger interactions on low-coordinated exposed Mg<sup>2+</sup> cations like the A sites of the (021) surface (see Fig. 2).

## HCN adsorption on the forsterite surfaces

The electrostatic potential maps (EPMs) superimposed to the ground state electron density were plotted for each forsterite surface model, as well as for HCN. Fig. 3 shows that, expectedly, HCN presents a clear dipole moment (experimental: 2.98 Debye, computed at PBE-*D*\*(*N*) level: 2.9 Debye), the H and N atoms determining the zone of positive and negative potentials, respectively. As regards the surfaces, the outermost Mg<sup>2+</sup> cations define the positive regions of electrostatic potential, while the outermost O atoms the negative potentials. Accordingly, Signorile *et al.*<sup>33</sup> pointed out that the exposed Mg<sup>2+</sup> cations have a Lewis acid character while the exposed O<sup>2−</sup> anions behave like Lewis bases. Therefore, the HCN adsorption was modelled considering the electrostatic potential complementarity rule, that is, by pointing the N-end of HCN towards an available Mg<sup>2+</sup> of the surface at a starting distance of about 2.0 Å. Moreover, HCN molecules were placed both on the top and on the bottom of the slabs to exploit the inversion operator during geometry optimizations to ensure zero dipole moment across the slab.

By proceeding this way, 16 different single adsorption complexes have been obtained with the six forsterite surfaces. Each adduct is named according to the surface Miller indices together with the adsorbing Mg<sup>2+</sup> cation label; for instance, (010) A represents the adduct obtained by placing HCN on the Mg<sup>2+</sup> A site of the (010) surface (see Fig. 2). Table 3 reports the dispersion-corrected adsorption energy (Δ*E*<sub>ads</sub>), the dispersion- and BSSE<sup>75–77</sup>-corrected adsorption energy (Δ*E*<sub>ads,disp</sub>), and the adsorption enthalpy at 0 K (Δ*H*<sub>ads</sub>(0)) of each optimized adduct. We point out that not always was possible to formally compute the BSSE, especially for the dissociative adsorption cases, where the proton is transferred to the surface (see Fig. 4). Nevertheless, a linear dependence (*R*<sup>2</sup> = 0.81, see Fig. S1, ESI†) between the adsorption energies and the corresponding BSSE values was obtained by plotting 13 representative points which have been used to extrapolate the BSSE values for those cases in which it was not possible to explicitly apply the counterpoise correction. Inter-cell lateral interactions between adsorbed molecules represent a spurious contribution to the Δ*E*<sub>ads</sub> due to the periodic approach. Indeed, when the computed lateral interaction absolute value (|Δ*E*<sub>L</sub>|) results higher than 3.0 kJ mol<sup>−1</sup>, supercell models are adopted to decrease the |Δ*E*<sub>L</sub>| contribution. This was done in 7 (out of 16) adsorption cases by doubling the unit cell along the *a* direction (*i.e.*, a 2 × 1 supercell), with the only exception of the (010) A case, where it was necessary to extend the cell along both *a* and *b* directions (*i.e.*, a 2 × 2 supercell). For some dissociative cases (namely, (101) C, (001) A, (021) A, B<sub>1</sub> and C) the instability of the SCF when computing the almost broken HCN in the absence of the surface, did not allow us to isolate the Δ*E*<sub>L</sub> contribution.

In 8 out of the 16 optimized adsorption complexes, HCN is molecularly adsorbed (*i.e.*, non-dissociative adsorption), interacting with one or more Mg<sup>2+</sup> cations through the N-end and, in most cases, the proton establishing hydrogen bonds (H-bonds) with surface O atoms, in consistency with the electrostatic potential features. The Δ*E*<sub>ads</sub> values for these cases span from





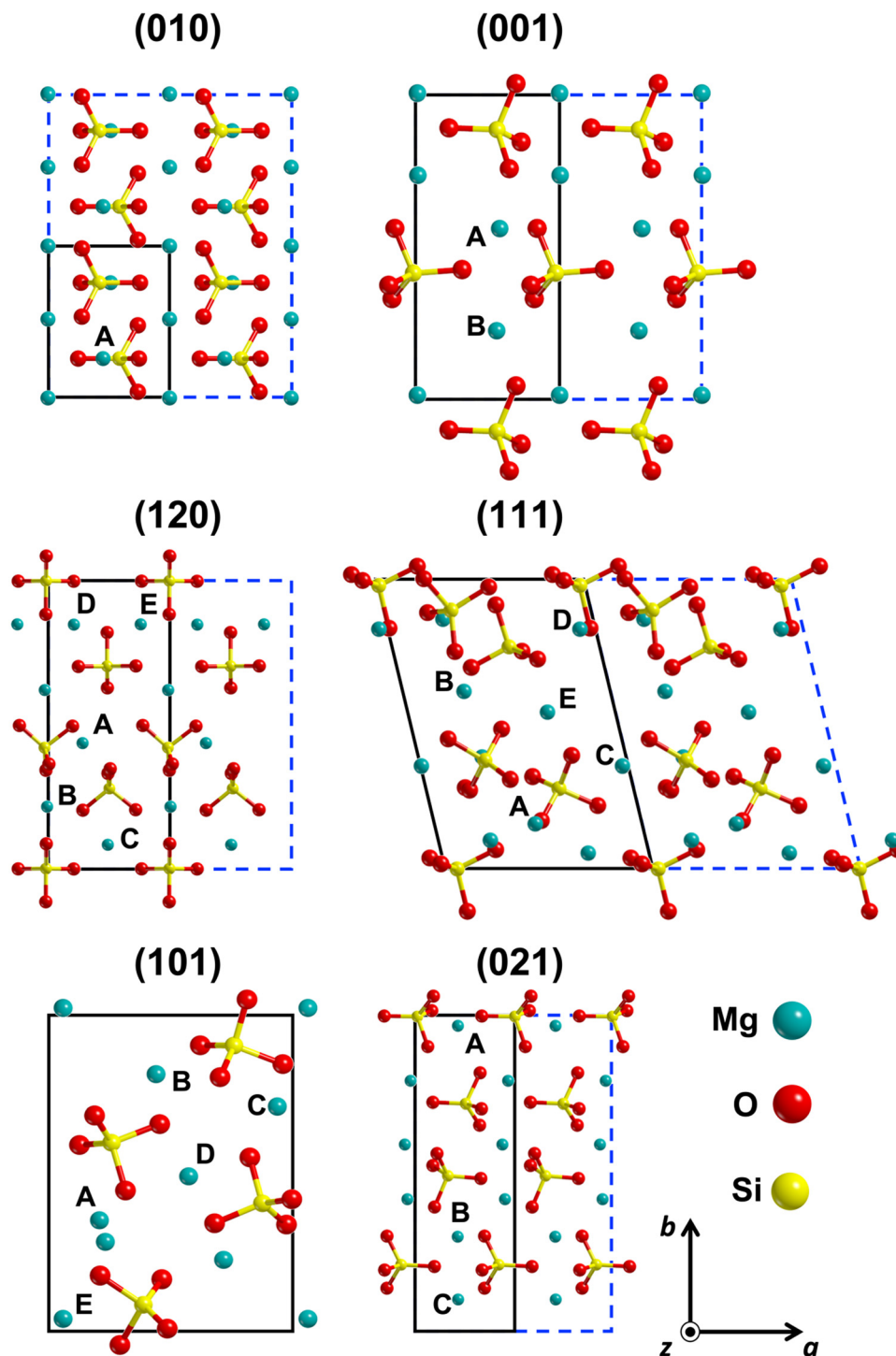


Fig. 2 Top views of the six forsterite surface models studied in this work (the surface (110) has not been considered). For sake of clarity, only the most exposed atomic layers are shown. The  $\text{Mg}^{2+}$  cations available for adsorption are labelled according to their  $z$ -coordinate, A being the most exposed ones. The unit cells are reported in black, while the supercells adopted for adsorbing HCN molecules are reported in blue dashed lines.

$-29.4$  to  $-127.7 \text{ kJ mol}^{-1}$ . In one case (the (111) D complex), HCN is chemisorbed by forming a C–O chemical bond between the C atom of HCN and the O atom of an exposed silicate (see Fig. 4). Even if the molecule does not dissociate, the computed adsorption energy results to be relatively high ( $\Delta E_{\text{ads}} = -221.5 \text{ kJ mol}^{-1}$ ) due to the new covalent bond formation.

In the remaining 8 cases, HCN adsorbs in a dissociative way, *i.e.* it deprotonates upon adsorption, transferring the proton to an available surface O atom. Dissociated adducts present larger  $\Delta E_{\text{ads}}$  values than the molecular ones (spanning the  $-135.0$  to  $-466.4 \text{ kJ mol}^{-1}$  range). Some of these dissociated structures show the newly formed  $\text{CN}^-$  anion to interact with the surface



**Table 2** Structural and energetic parameters for the seven surface slab models: cell parameters ( $a$  and  $b$ , Å), cell angle ( $\gamma$ , degrees), surface unit cell area ( $A$ , Å<sup>2</sup>), surface energy ( $E_s$ , J m<sup>-2</sup>), and morphological relevant index (MRI, see text for more details). Comparison of the  $E_s$  and MRI values with those of Zamirri *et al.* calculated at B3LYP- $D^*$  (% $\Delta$  and  $\Delta$ , respectively) is also reported

(hkl)	Cell parameters				$E_s$			MRI		
	$a$	$b$	$\gamma$	$A$	This work	Zamirri <sup>a</sup>	% $\Delta$	This work	Zamirri <sup>a</sup>	$\Delta$
(010)	4.801	6.008	90.0	28.84	1.38	1.44	-3.9	21.3	23.7	-2.4
(120)	6.008	14.017	90.0	84.21	1.52	1.68	-9.4	33.0	29.6	3.4
(101)	7.691	10.212	90.0	78.53	1.78	1.96	-9.2	21.8	20.6	1.2
(001)	4.801	10.212	90.0	49.03	1.85	1.98	-6.6	15.5	19.7	-4.2
(111)	7.691	11.284	105.4	83.67	1.99	2.19	-8.9	3.3	2.4	0.9
(021)	4.801	15.769	90.0	75.71	2.06	2.24	-7.9	5.1	3.5	1.6
(110)	6.008	11.284	90.0	67.79	2.34	2.46	-4.9	0.0	0.0	0.0

<sup>a</sup> Zamirri *et al.*<sup>53</sup>

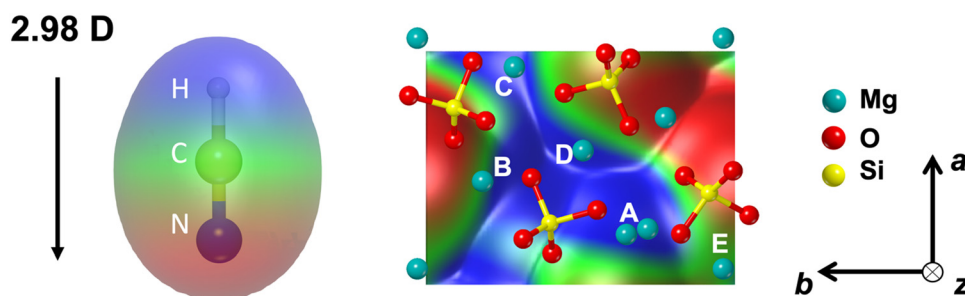


**Fig. 3** Electrostatic potential maps (EPMs) superimposed to the ground electron density for the HCN molecule (left) and the (101) surface (right), computed at the PBE- $D^*(N)$  level. The isodensity value for the electron density was set to  $10^{-6}$  a.u. Colour code: blue, +0.02 a.u.; green, 0.0 a.u.; red, -0.02 a.u. The black arrow on the left reports the dipole moment of the isolated HCN molecule.  $Mg^{2+}$  cations are labelled according to their  $z$ -coordinate, A being the most exposed. The EPMs images were generated with VMD software.

**Table 3** Dispersion-corrected adsorption energies ( $\Delta E_{ads,disp}$ ), dispersion contributions to the adsorption energy ( $\Delta D^*(N)$ ), dispersion- and BSSE-corrected adsorption energies ( $\Delta E_{ads}$ ), and enthalpies of adsorption at 0 K ( $\Delta H_{ads}(0)$ ). All energies are in kJ mol<sup>-1</sup>

(hkl)	Site	Type	$\Delta E_{ads,disp}$	$\Delta D^*(N)$	$\Delta E_{ads}$	$\Delta H_{ads}(0)$
(010)	A	M	-134.9	-17.2	-101.0	-96.9
(120)	A	M	-165.0	-15.2	-127.7	-119.9
	B	M	-60.8	-14.3	-29.4	-21.0
	C	M	-104.8	-19.6	-63.1	-52.1
(101)	A	D	-219.4	-18.4	-174.5	-163.9
	B	M	-106.1	-18.2	-68.6	-61.8
	C	D	-226.6	-22.3	-181.2	-171.9
(001)	A	D	-273.3	-17.4	-223.7	-202.4
	B	M	-114.2	-20.1	-77.4	-58.8
(111)	A	M	-155.4	-19.6	-105.4	-96.6
	B	D	-272.9	-22.1	-223.3	-207.8
	D	M	-271.0	-19.1	-221.5	-194.7
(021)	A	D	-540.9	-24.2	-466.4	-447.8
	B <sub>1</sub>	D	-187.5	-20.1	-145.8	-133.9
	B <sub>2</sub>	D	-175.8	-16.9	-135.0	-123.9
	C	D	-186.4	-19.2	-143.7	-137.0

through a Mg-N dative covalent bond and a C...HO H-bond, with  $\Delta E_{ads}$  values being between -135.0 and -223.3 kJ mol<sup>-1</sup>. In other cases, the CN<sup>-</sup> anion prefers to establish additional interactions with surface  $Mg^{2+}$  cations, involving simultaneously different Mg-N and Mg-C dative bonds, thus presenting larger  $\Delta E_{ads}$  values (between -181.2 and -466.4 kJ mol<sup>-1</sup>). For these cases, the C...HO H-bonds are not formed, but the

newly formed Si-OH groups establish H-bonds with other surface O atoms. One of the most representative cases is the (021) A (see Fig. 4), where CN<sup>-</sup> strongly bridges three  $Mg^{2+}$  cations. This structure presents the largest  $\Delta E_{ads}$  value ( $\Delta E_{ads} = -466.4$  kJ mol<sup>-1</sup>). This is due to three main features: (i) the low stability of the surface ( $E_s = 2.06$  J m<sup>-2</sup>), which renders the outermost atoms very reactive enhancing their adsorbent properties (see Fig. 4 and Fig. S14, ESI<sup>†</sup>), (ii) the simultaneous three CN-Mg interactions and (iii) the formation of a strong H-bond between the surface SiOH group and an exposed surface O atom.

A linear plot between the  $\Delta E_{ads}$  values and the Mg-N/Mg-C distances is not possible, especially for the dissociated cases, due to the variety in the number of Mg/CN interactions. A more reliable descriptor to rationalize the energetics of the HCN adsorption is the contribution of dispersion forces to  $\Delta E_{ads}$  and the surfaces stability, as discussed in the next section.

### Role of dispersion and surface stability

Here we discuss the relationships between the stability of the surfaces and the HCN/surface dispersion-based interactions to further rationalize the computed  $\Delta E_{ads}$  values.

The surface stability (see values in Table 2 and Fig. 5B) is quantified by the surface energy ( $E_s$ ), which in turn is partly determined by the amount of coordinatively unsaturated  $Mg^{2+}$  ions, in such a way that, the higher the surface energy, the less



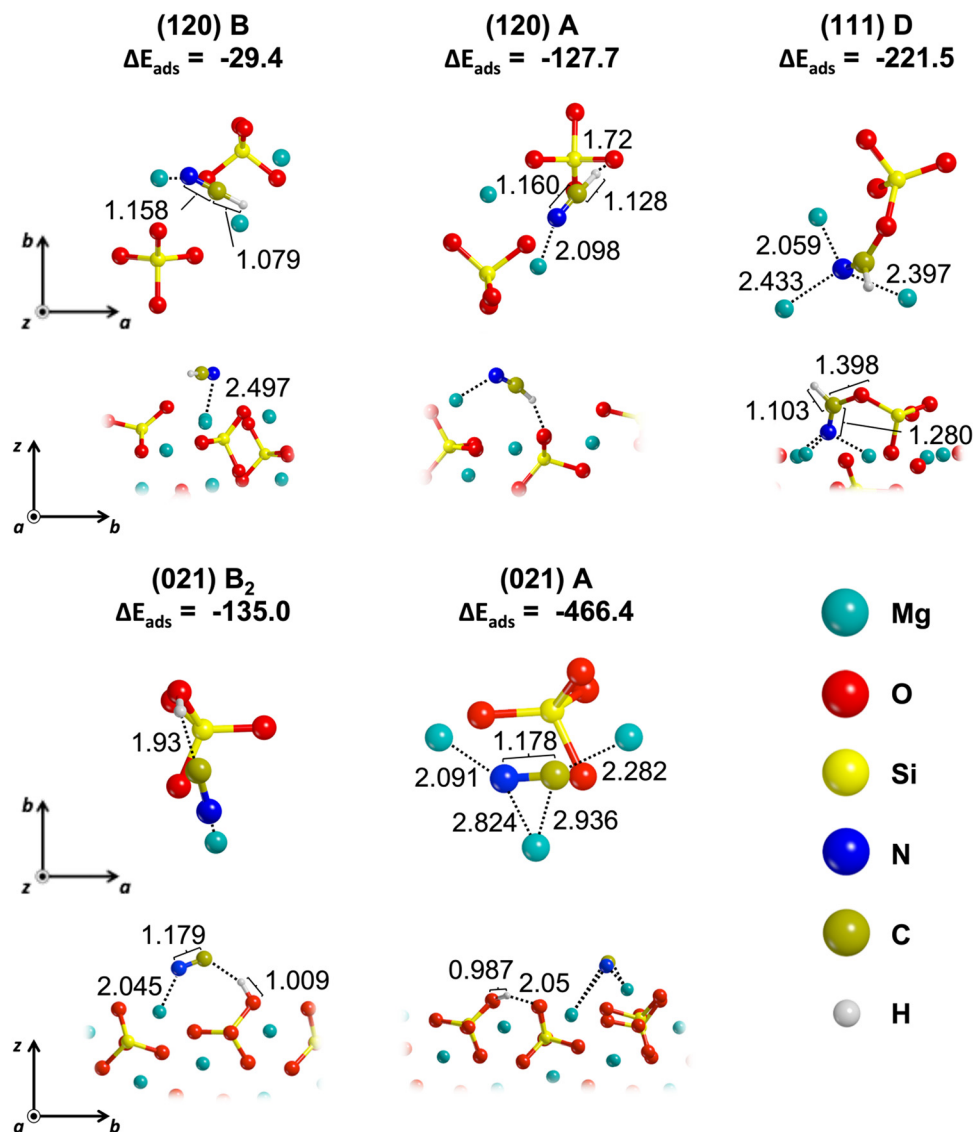


Fig. 4 Top and side views of 5 representative optimized structures of HCN adsorption on the different forsterite surfaces. The first row shows the less and more stable cases for the molecular adsorption (*i.e.*, (120) B and A), together with the (111) D case, where the C–O bond formation occurs. The second row reports the least and most stable cases for the dissociative adsorptions (*i.e.*, (021) B<sub>2</sub> and A). The computed  $\Delta E_{\text{ads}}$  (corrected for both dispersion and BSSE) are reported in  $\text{kJ mol}^{-1}$ . All distances are in Å.

stable (and consequently the more reactive) the surface. The relative surface stabilities (see above) allow explaining the spontaneous HCN dissociation upon adsorption in the four less stable surfaces, namely, (101), (001), (111), (021). For these cases, the exposed  $\text{O}^{2-}$  anions present an enhanced basicity that induces HCN deprotonation, due to the surface instability.<sup>33</sup> Despite this consistency, by comparing Fig. 5A (the average of the calculated  $|\Delta E_{\text{ads}}|$  values for each surface) and Fig. 5B (the  $E_{\text{s}}$  values for each surface), it is difficult to find a clear quantitative correlation, even if the trend of the two charts is somehow similar. This is because the overall surface stability of a specific slab depends on many variables (*e.g.*, the degree of unsaturation of the  $\text{Mg}^{2+}$  cations, the exposure to the surface of the  $\text{O}^{2-}$  anions), conditioning the HCN/surface interactions.

As for dispersive forces, Fig. 5C reports the  $|\Delta E_{\text{ads}}|$  values as a function of the dispersion contribution (disp.%) showing higher  $|\Delta E_{\text{ads}}|$  values corresponding to lower percentages of dispersive contributions. The two quantities can be well correlated ( $R^2 = 0.96$ ) by a non-linear plot given by a power function of the disp.% contribution. This trend suggests that molecular adsorptions (which in turn are those presenting the less favourable  $\Delta E_{\text{ads}}$  values) are usually more dominated by weak dispersive forces ( $48.8\% < \text{disp.} < 8.1\%$ ). On the other hand, dissociative adsorptions are governed by covalent/ionic forces ( $12.5\% < \text{disp.} < 5.2\%$ ) such as Mg–N and Mg–C dative covalent bonds and strong H-bonds.

#### Dissociation of molecularly adsorbed HCN molecules

As mentioned in the Introduction, the prebiotic polymerization of HCN is strongly hindered in the gas phase under interstellar



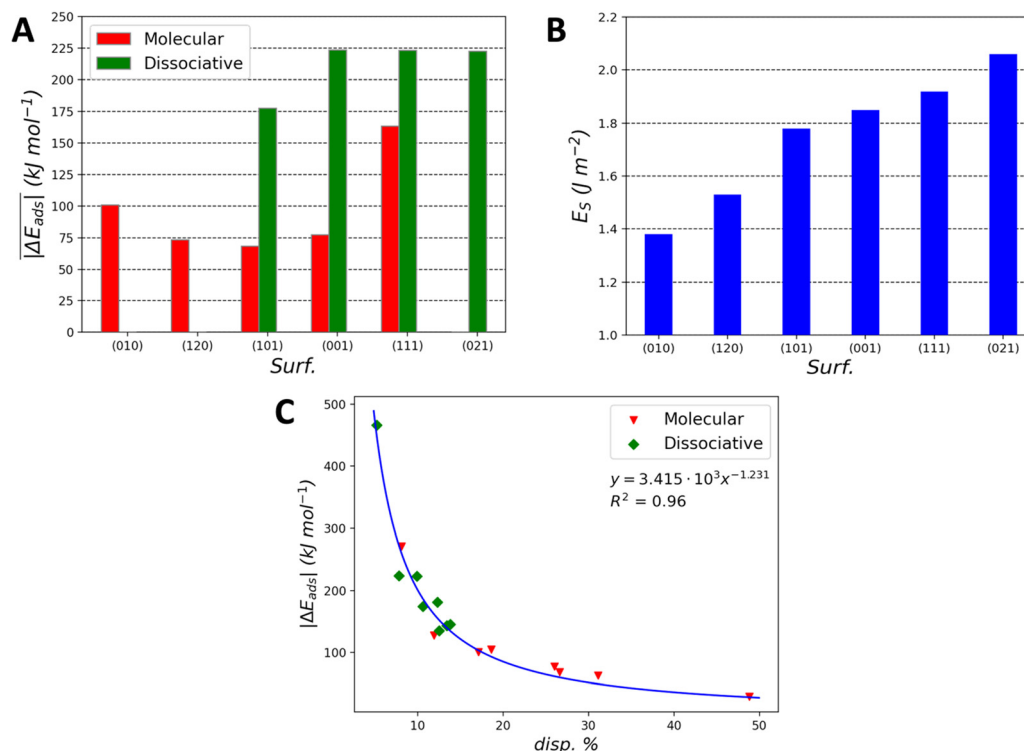


Fig. 5 (A) Average of the calculated  $|\Delta E_{\text{ads}}|$  values based on all the adsorptions on each forsterite surface. (B) Calculated surface energies ( $E_s$ ) for each surface (see Table 2). (C) Correlation between calculated averaged- $|\Delta E_{\text{ads}}|$  values with the corresponding percentage dispersion contributions, provided by the  $D^*(N)$  term.

conditions,<sup>30</sup> while it is more facilitated in the condensed phase, in the presence of a basic catalyst and at higher temperatures.<sup>17,29,31,32</sup> Since the formation of  $\text{CN}^-$  anions is considered as the real trigger to the reaction, we explored the deprotonation channels of molecularly adsorbed HCN in case that a kinetic energy barrier is present. The reactants (namely, the molecular adsorption complexes), the TSs and the products of proton transfers from HCN to the closest outermost  $\text{O}^{2-}$  anion of forsterite (see Fig. 6 as a test case) were localized for 5 (out of 8) non-dissociative cases. For the remaining three cases, we could not localize minima on the potential energy surface corresponding to stable deprotonated structures and every

deprotonated initial guess showed the proton going back to covalently bound the  $\text{CN}^-$ .

Table 4 reports the relevant thermodynamic and kinetic parameters (*i.e.*, activation barriers, reaction energies, and kinetic and equilibrium constants) of the dissociation process for the 5 cases, considering different temperatures (10, 50, 150, 200 and 300 K). We report the values at these temperatures as representative of different astrophysical environments: 10 K as the typical temperature of dark clouds, 50 and 150 K for hot cores/corinos and outer regions of proto-planetary disks and 200 and 300 K as temperatures of planetary atmospheres and those to which the system is exposed in the case of asteroids and comets when passing close to stars.

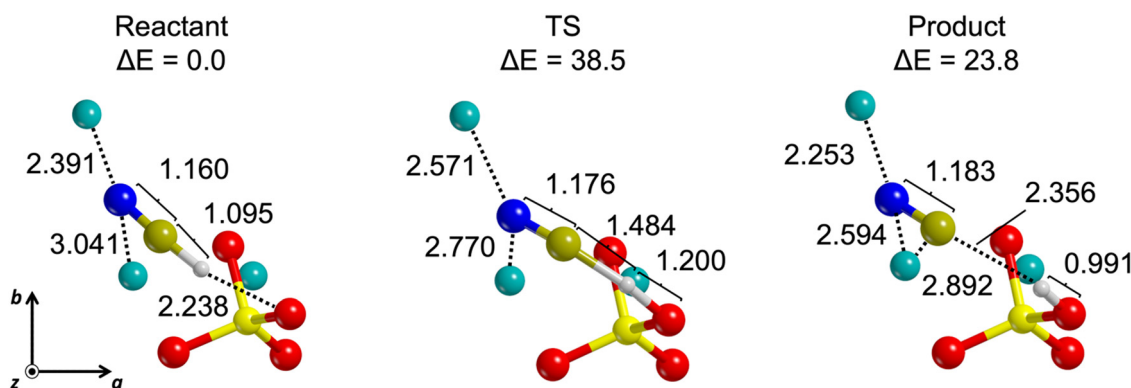


Fig. 6 Illustrative example of HCN deprotonation channel of the (101) B adsorption complex: top view of reactants, transition state (TS) and products. Relative PBE- $D^*(N)$  potential energies ( $\Delta E$ ) are referred to the reactant energy. Energy units in  $\text{kJ mol}^{-1}$ , distances in Å.



**Table 4** Thermodynamic and kinetic parameters for the five cases of activated dissociation of adsorbed HCN molecules at different temperatures in K. Reaction enthalpy ( $\Delta H^*$ ), Gibbs free reaction energy ( $\Delta G^*$ ), activation enthalpy ( $\Delta H^\ddagger$ ) and Gibbs free activation energy ( $\Delta G^\ddagger$ ) are in  $\text{kJ mol}^{-1}$ . Kinetic constants accounting for tunneling effects ( $k_{\text{full}}$ ) are in  $\text{s}^{-1}$ . Thermodynamic equilibrium constants are reported as  $K^{\text{eq}}$

Case	t.k. param.	Temp. (K)				
		10	50	150	200	300
(010) A	$\Delta H^*$	6.1	6.1	6.3	6.6	7.2
	$\Delta G^*$	6.1	6.2	6.2	6.1	5.8
	$\Delta H^\ddagger$	64.5	64.4	63.9	63.6	62.9
	$\Delta G^\ddagger$	64.5	64.5	64.9	65.3	66.3
	$k_{\text{full}}$	$1.1 \times 10^{-45}$	$5.0 \times 10^{-34}$	$2.3 \times 10^{-10}$	$6.3 \times 10^{-05}$	$2.2 \times 10^{01}$
	$K^{\text{eq}}$	$7.6 \times 10^{-33}$	$3.6 \times 10^{-07}$	$6.9 \times 10^{-03}$	$2.5 \times 10^{-02}$	$9.8 \times 10^{-02}$
(120) B	$\Delta H^*$	−152.4	−153.4	−156.4	−157.0	−157.6
	$\Delta G^*$	−152.3	−151.5	−145.5	−141.8	−134.0
	$\Delta H^\ddagger$	27.0	26.3	23.9	23.0	20.9
	$\Delta G^\ddagger$	27.1	27.8	32.3	35.2	41.8
	$k_{\text{full}}$	$1.2 \times 10^{-58}$	$3.9 \times 10^{-23}$	$1.1 \times 10^{00}$	$7.5 \times 10^{02}$	$5.3 \times 10^{05}$
	$K^{\text{eq}}$	$4.0 \times 10^{265}$	$2.1 \times 10^{158}$	$4.5 \times 10^{50}$	$1.0 \times 10^{37}$	$2.1 \times 10^{23}$
(120) C	$\Delta H^*$	−7.6	−7.8	−8.1	−8.2	−8.5
	$\Delta G^*$	−7.6	−7.4	−6.9	−6.5	−6.0
	$\Delta H^\ddagger$	2.5	2.2	0.7	−0.1	−2.0
	$\Delta G^\ddagger$	2.5	2.7	4.7	6.2	9.7
	$k_{\text{full}}$	$2.6 \times 10^{09}$	$5.1 \times 10^{10}$	$3.1 \times 10^{11}$	$4.5 \times 10^{11}$	$6.6 \times 10^{11}$
	$K^{\text{eq}}$	$6.5 \times 10^{39}$	$6.4 \times 10^{07}$	$1.9 \times 10^{02}$	37.0	7.0
(101) B	$\Delta H^*$	22.9	23.0	23.9	24.4	25.2
	$\Delta G^*$	22.9	22.8	22.0	21.3	19.5
	$\Delta H^\ddagger$	17.6	17.6	16.9	16.4	15.3
	$\Delta G^\ddagger$	17.6	17.3	17.6	17.9	19.0
	$k_{\text{full}}$	$5.0 \times 10^{-04}$	$2.8 \times 10^{-01}$	$1.6 \times 10^{04}$	$9.1 \times 10^{05}$	$1.2 \times 10^{08}$
	$K^{\text{eq}}$	$3.6 \times 10^{-120}$	$1.5 \times 10^{-24}$	$2.2 \times 10^{-08}$	$2.8 \times 10^{-06}$	$4.0 \times 10^{-04}$
(111) A	$\Delta H^*$	−13.8	−14.2	−13.8	−13.2	−12.2
	$\Delta G^*$	−13.8	−13.6	−12.3	−11.9	−11.5
	$\Delta H^\ddagger$	14.8	14.5	13.5	12.9	11.5
	$\Delta G^\ddagger$	14.8	14.9	16.3	17.3	19.7
	$k_{\text{full}}$	$1.3 \times 10^{02}$	$3.9 \times 10^{03}$	$7.2 \times 10^{05}$	$9.3 \times 10^{06}$	$3.4 \times 10^{08}$
	$K^{\text{eq}}$	$1.8 \times 10^{72}$	$1.6 \times 10^{14}$	$2.0 \times 10^{04}$	$1.3 \times 10^{03}$	$1.0 \times 10^{02}$

Three out of 5 cases (namely, (120) B, (120) C, and (111) A) present exergonic reactions, while the other two (namely, (010) A and (101) B) are endergonic. It follows that equilibrium constants ( $K^{\text{eq}}$ ) for the former are  $>0$  at every considered temperature while the opposite occurs for the latter. For all the cases the decrease of the activation enthalpy with temperature is eroded by the entropic effects. The same happens to the reaction enthalpies: the spontaneity of the exergonic dissociations on the (120) B, (120) C and (111) A cases decreases as the temperature increases, while the (010) A and (101) B adducts (those with positive free energy reactions) follow the opposite trend. Nevertheless, no inversion of stability is observed in any case.

The (120) B is a special case, because the dissociation of the adsorbed molecule leads to a considerably favourable reaction energy ( $\Delta H^*(10 \text{ K}) = -152.4 \text{ kJ mol}^{-1}$ ) and to strong entropic effects. This is due to a rearrangement of the  $\text{CN}^-$  anion on the surface (see Fig. S19, ESI†), where the  $\text{CN}^-$  species bridges between two  $\text{Mg}^{2+}$  cations, thus forming a strong interaction with the surface. The high stabilization can be explained when considering the non-dissociated starting structure (see Fig. 4), where the HCN weakly interacts with only one surface  $\text{Mg}^{2+}$  without forming appreciable H-bonds with  $\text{O}^{2-}$  anions.

This initial structure is the adduct with the least favourable adsorption energy ( $\Delta E_{\text{ads}} = -29.4 \text{ kJ mol}^{-1}$ ) so that, upon dissociation, the system gains large stabilization.

Kinetic constants have been computed through the RRKM scheme, taking into account tunnelling effects (see Fig. 7). In Table S1 (ESI†) the comparison between the kinetic constants with ( $k_{\text{full}}$ ) and without accounting for tunnelling ( $k_{\text{class}}$ ) is reported in detail. In general, tunnelling starts to be relevant at 150 K for almost all cases and become dominant as the temperature decreases, increasing the reaction rate of several orders of magnitude at  $T \leq 50 \text{ K}$ .

At 10 K, the deprotonated forms of cases (120) C and (111) A are both thermodynamically and kinetically favoured. If we also consider the barrier-less dissociative adsorption previously discussed, 10 out of the total 16 adsorption cases confirm that the deprotonated form of HCN is more abundant in the ISM than HCN. If we consider the latest stages of a planetary system formation (proto-planetary disks, planetesimals, comets, asteroids, and satellites) only two cases are thermodynamically unfavoured, *i.e.* (010) A and (101) B, while all the others result in the deprotonation of HCN.

The results exposed up to now refer to HCN-forsterite systems, that is, only the crystalline pure Mg-silicate is considered.



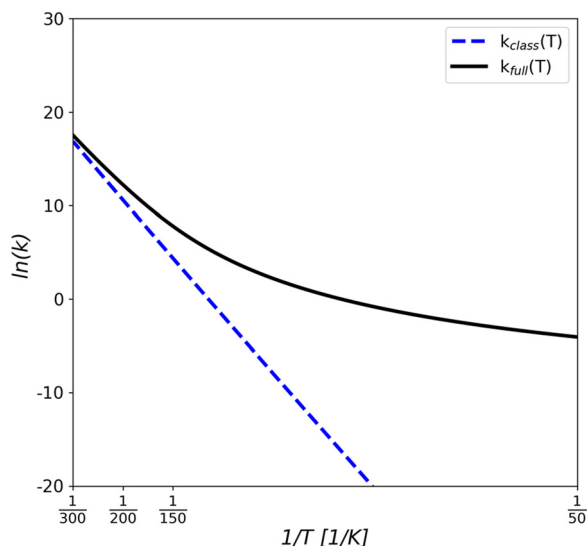


Fig. 7 Arrhenius plot of the calculated rate constants,  $k_{full}$  (black line) and  $k_{class}$  (blue dashed line), for the HCN dissociation from the (101) B adsorption complex between 50 and 300 K. The units of the rate constants are in  $s^{-1}$ .

If we consider interstellar dust grains, the crystalline phase is thought to constitute only around 5% of the silicates in the grain

cores, the amorphous phase being dominant.<sup>63</sup> Even if the crystalline phase tends to become dominant during a planetary systems formation,<sup>93</sup> it surely represents just a fraction of the silicates in the environments we have considered. Amorphous silicates differ from the crystalline one in the basicity of the exposed  $O^{2-}$ , which are averagely more basic in the former than in the latter.<sup>33</sup> This is due to the formation of MgO polymers in the amorphous phase, whose exposed  $O^{2-}$  are more basic than those belonging to  $SiO_4^{4-}$  units.<sup>94</sup> If we consider the high degree of deprotonation in the HCN-forsterite system, we can then suppose that amorphous silicates and MgO would deprotonate adsorbed HCN even more efficiently. This would lead to a greater quantity of  $CN^-$  and, thus, to a more efficient catalysis towards the HCN polymerization. Indeed, it was experimentally observed by Santalucia *et al.*<sup>31</sup> that the reactivity of HCN on these materials increases in the order: forsterite  $\rightarrow$  amorphous silicate  $\rightarrow$  MgO.

### IR spectral features of adsorbed HCN molecules

The vibrational frequencies were computed for all the adsorption complexes, including the dissociated ones. The scaled stretching frequencies of the  $C\equiv N$  and  $C-H$  have been compared with those computed for the HCN molecule in the gas phase to evaluate the perturbation of these chemical bonds

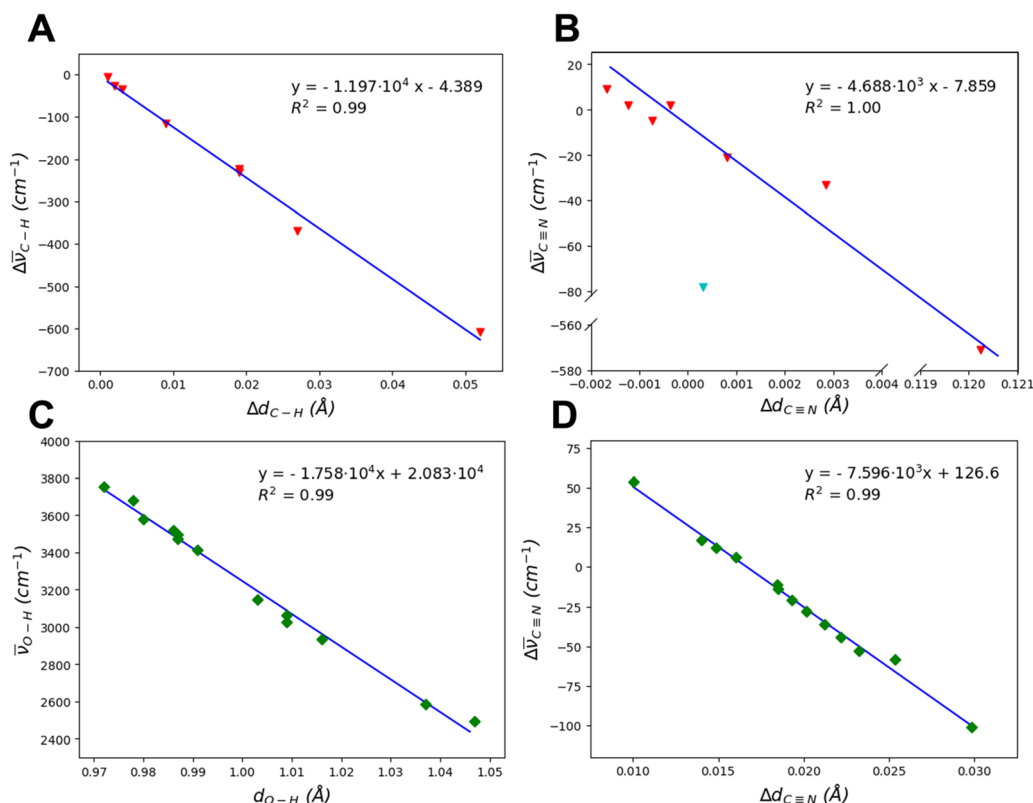


Fig. 8 (A) and (B) Correlation between the C–H and C≡N bond length variations ( $\Delta d_{C-H}$  and  $\Delta d_{C\equiv N}$ ) and corresponding computed stretching frequency shifts ( $\Delta \nu_{C-H}$  and  $\Delta \nu_{C\equiv N}$ ) with respect to the isolated HCN molecule for non-dissociative adsorptions. The outlier point in graph B (reported in cyan), represents the (120) A case (see text for more details). (C) correlation between the O–H bond lengths ( $d_{O-H}$ ) and the corresponding stretching frequency ( $\nu_{O-H}$ ) for the dissociative adsorptions. (D) correlation between the C≡N bond length variation ( $\Delta d_{C\equiv N}$ ) and the computed frequency shift ( $\Delta \nu_{C\equiv N}$ ) with respect to the isolated HCN molecule for dissociative adsorptions.

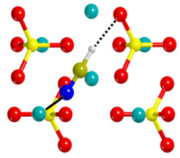
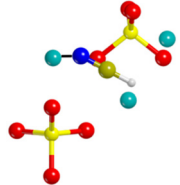
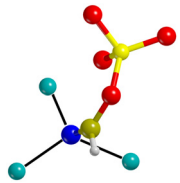
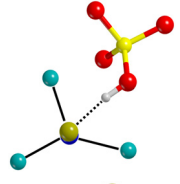
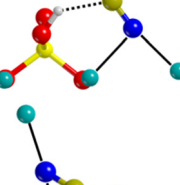
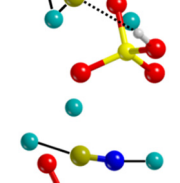
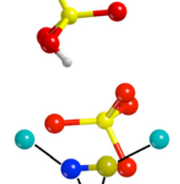
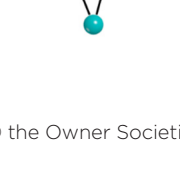


upon HCN adsorption (see Tables S2–S4, ESI† for full details about bond distances and corresponding frequencies).

Fig. 8A and B plot the variation of the C–H and C≡N bond lengths against the corresponding frequency shift values with respect the gas-phase molecule. The correlation is very good, with the only exception of the C≡N bond in (120) A.

This adduct (see Fig. 4) presents high bathochromic shifts ( $\Delta\nu_{\text{C}\equiv\text{N}} = -78 \text{ cm}^{-1}$  and  $\Delta\nu_{\text{C-H}} = -609 \text{ cm}^{-1}$ , see Table S2, ESI†) correlated to the strong interactions due to the adsorption, *i.e.* short O···HC and Mg–N distance (1.721 and 2.098 Å, respectively). As expected, the adducts presenting the largest adsorption energies are the most perturbed by the adsorption

**Table 5** Main vibrational and structural features of the eight different classes of HCN/forsterite adsorption complexes. The range of computed frequencies are reported for C≡N and C–H bonds, together with the Mg–N and Mg–C distances and the H-bonds distances given either by molecular HCN or by silanols formed upon dissociation

Class	Structure	Features	Description
I		$\Delta\nu_{\text{C}\equiv\text{N}} = -78 \text{ to } -5 \text{ cm}^{-1}$ $\Delta\nu_{\text{C-H}} = -609 \text{ to } -116 \text{ cm}^{-1}$ $d_{\text{Mg-N}} = 2.098\text{--}2.391 \text{ Å}$ $d_{\text{O}\cdots\text{HC}} = 1.721\text{--}2.554 \text{ Å}$	Molecular adsorption Single NC–H···O–SiO <sub>3</sub> H-bond Single HCN–Mg dative bond
II		$\Delta\nu_{\text{C}\equiv\text{N}} = 2\text{--}9 \text{ cm}^{-1}$ $\Delta\nu_{\text{C-H}} = -35 \text{ to } -6 \text{ cm}^{-1}$ $d_{\text{Mg-N}} = 2.173\text{--}2.503 \text{ Å}$ $d_{\text{O}\cdots\text{HC}} = 2.446\text{--}2.845 \text{ Å}$	Molecular adsorption H-bond weak or null Single HCN–Mg dative bond
III		$\Delta\nu_{\text{C}\equiv\text{N}} = -571 \text{ cm}^{-1}$ $\Delta\nu_{\text{C-H}} = -369 \text{ cm}^{-1}$ $d_{\text{Mg-N}} = 2.059\text{--}2.433 \text{ Å}$	Molecular adsorption Change of hybridization of C (sp to sp <sup>2</sup> ) Conversion of C≡N to C=N
IV		$\Delta\nu_{\text{C}\equiv\text{N}} = -101 \text{ cm}^{-1}$ $d_{\text{Mg-N}} = 2.008\text{--}2.374 \text{ Å}$ $d_{\text{OH}\cdots\text{CN}} = 2.084 \text{ Å}$	Dissociative adsorption Triple Mg–NC coordination
V		$\Delta\nu_{\text{C}\equiv\text{N}} = -44 \text{ to } -11 \text{ cm}^{-1}$ $d_{\text{Mg-N}} = 2.008\text{--}2.264 \text{ Å}$ $d_{\text{OH}\cdots\text{CN}} = 1.757\text{--}1.927 \text{ Å}$	Dissociative adsorption Single or double Mg–NC <sup>−</sup> coordination Single NC <sup>−</sup> ···H–OSi H-bond
VI		$\Delta\nu_{\text{C}\equiv\text{N}} = -58 \text{ to } -53 \text{ cm}^{-1}$ $d_{\text{Mg-N}} = 2.129\text{--}2.317 \text{ Å}$ $d_{\text{Mg-C}} = 2.747\text{--}2.892 \text{ Å}$ $d_{\text{OH}\cdots\text{XN}} = 2.071\text{--}2.356 \text{ Å}$ (X = C or O)	Dissociative adsorption Single Mg–N + single Mg–CN <sup>−</sup> lateral bond
VII		$\Delta\nu_{\text{C}\equiv\text{N}} = 6\text{--}54 \text{ cm}^{-1}$ $d_{\text{Mg-N}} = 2.078\text{--}2.130 \text{ Å}$ $d_{\text{Mg-C}} = 2.127\text{--}2.303 \text{ Å}$ $d_{\text{OH}\cdots\text{OSi}} \geq 1.560 \text{ Å}$	Dissociative adsorption CN <sup>−</sup> bridging between 2 Mg
VIII		$\Delta\nu_{\text{C}\equiv\text{N}} = -14 \text{ cm}^{-1}$ $d_{\text{Mg-N}} = 2.091\text{--}2.824 \text{ Å}$ $d_{\text{Mg-C}} = 2.282\text{--}2.936 \text{ Å}$ $d_{\text{OH}\cdots\text{OSi}} = 2.053 \text{ Å}$	Dissociative adsorption CN <sup>−</sup> bridging between 2 Mg + single Mg–CN <sup>−</sup> lateral bond



and, accordingly, those with the largest frequency shifts. Thus, the strong interaction with the surface and, in the specific, the electron donation from the lone pair on the N to the  $\text{Mg}^{2+}$  cations (dative Mg–N bond) cause a weakening of the CN bond. As regards the C–H bond, its vibrational perturbation is generally driven by the H donation towards surface O atoms. However, there is no direct correlation between the Mg–N distances and  $\Delta\nu_{\text{C}\equiv\text{N}}$  and between  $\text{O}\cdots\text{HC}$  distances and  $\Delta\nu_{\text{C-H}}$ , due to the variable number of simultaneous Mg–N and  $\text{O}\cdots\text{HC}$  interactions occurring in the different adsorption complexes.

For the dissociative cases, the O–H bond lengths and stretching frequencies follow a good correlation as well, as shown in Fig. 8C. As expected, larger shifts are observed when the newly formed SiOH group establishes H-bonds with the C atom of  $\text{CN}^-$  rather than with another surface O atom. This is consistent with the fact that  $\text{CN}^-$  carries a negative net charge and that it has more mobility with respect to bulky silicates, thus maximizing the efficiency of the H-bond interaction. Nevertheless, this trend is not followed when  $\text{CN}^-$  is strongly bound by more than one  $\text{Mg}^{2+}$ , as they compensate its negative charge and prevent its displacement towards the silanol ((111) B case, see Table 5, class IV, and Fig. S12, ESI†). The CN distances and the stretching frequency shifts (see Fig. 8D) show a good correlation as well. In these cases, however, we observe both bathochromic and hypsochromic shifts with respect to the HCN molecule, which depend on the adsorption modes between the  $\text{CN}^-$  and the surface.

Basing on the common structural and spectroscopic features, the HCN/surface interactions can be grouped in 8 different adsorption complex classes, which are described in Table 5. Classes I, II, and III include different situations of molecular adsorption. In class I the appreciable H-bond donations occurring between HCN and the O atoms of the surface cause an appreciable activation of the C–H bond ( $\Delta\nu_{\text{C-H}} = -609$  to  $-116\text{ cm}^{-1}$ ) together with bathochromic shifts of the  $\text{C}\equiv\text{N}$  stretching frequencies ( $\Delta\nu_{\text{C}\equiv\text{N}} = -78$  to  $-5\text{ cm}^{-1}$ ). In class II the  $\text{H}\cdots\text{O-Si}$  donation is less appreciable or even null: weaker effects on the C–H bond and slight hypsochromic shifts of the  $\text{C}\equiv\text{N}$  frequency are observed ( $\Delta\nu_{\text{C-H}} = -35$  to  $-6\text{ cm}^{-1}$ ,  $\Delta\nu_{\text{C}\equiv\text{N}} = 2$ – $9\text{ cm}^{-1}$ ). Class III only includes the (111) D case, where the new C–O bond formation implies a change of hybridization of the C atom and a decrease in the bond order of the CN. It follows that important bathochromic shifts of both the CH and the CN frequency are observed ( $\Delta\nu_{\text{C-H}} = -369\text{ cm}^{-1}$ ,  $\Delta\nu_{\text{C}\equiv\text{N}} = -571\text{ cm}^{-1}$ ).

Classes IV to VIII include dissociative adsorptions. The largest bathochromic shifts are observed when the C atom of  $\text{CN}^-$  works as H-bond acceptor from the new formed silanols. This is the case for classes IV, V and VI, for which the bathochromic shifts of the CN stretching frequencies span from  $-101$  to  $-11\text{ cm}^{-1}$ . A minor effect to these red-shifts can also be ascribed to  $\sigma$ -donations occurring from the bonding molecular orbitals (MOs)  $2\pi$  HOMO–1 ( $E = -0.539\text{ eV}$ ) of the  $\text{CN}^-$  to the empty s orbitals of the exposed  $\text{Mg}^{2+}$ . In classes VII and VIII, instead, the  $\text{CN}^-$  does not interact with exposed silanols but it maximizes the number of dative bonds with exposed  $\text{Mg}^{2+}$

cations. In fact, class VII involves a bridged Mg–CN–Mg motif resulting in hypsochromic shifts for CN ( $\Delta\nu_{\text{C}\equiv\text{N}} = 6$ – $54\text{ cm}^{-1}$ ), which can be attributed to the interaction between the electric field of the surface and the dipole moment of the molecule (Stark effect)<sup>95–97</sup> and, in a minor extent, to the depopulation of the HOMO ( $E = 0.650\text{ eV}$ ) of  $\text{CN}^-$  by  $\sigma$ -donation to the empty s-orbitals of  $\text{Mg}^{2+}$ . This class is the one that better fits the  $2130\text{ cm}^{-1}$  signal observed by Santalucia *et al.*<sup>31</sup> at 150 K, which the authors attribute to deprotonated  $\text{CN}^-$  anions adsorbed on forsterite surfaces. Lastly, in class VIII a triple Mg–CN interaction results in a weak bathochromic shift ( $\Delta\nu_{\text{C}\equiv\text{N}} = -14\text{ cm}^{-1}$ ), likely due to a balance between the opposite blue-shifting contribution of the Stark effect and the red-shifting  $\sigma$ -donation from the HOMO–1 orbital of  $\text{CN}^-$  to the empty s-orbitals of  $\text{Mg}^{2+}$ .

## Conclusions

In this work, the adsorption of hydrogen cyanide (HCN) on different silicate forsterite ( $\text{Mg}_2\text{SiO}_4$ ) surfaces (*i.e.*, the crystal-line slab models of the (010), (120), (101), (001), (111) and (021) surfaces) has been investigated by means of periodic DFT simulations.

The interaction of HCN molecules with the forsterite surfaces resulted in 16 different adducts. Adsorption at 0 K can take place either in molecular (8 cases) and dissociative (8 cases) ways, the latter providing more favourable adsorption energies ( $-135.0\text{ kJ mol}^{-1} > \Delta E_{\text{ads}} > -466.4\text{ kJ mol}^{-1}$ ) than the former ( $-29.4\text{ kJ mol}^{-1} > \Delta E_{\text{ads}} > -221.5\text{ kJ mol}^{-1}$ ).

Dissociation reactions from molecularly adsorbed complexes have been studied by localizing the transition states of the proton transfer from HCN to nearby surface O atoms. Out of 8 non-dissociated initial systems, 3 have been found to result in stable dissociated structures through exergonic processes. Activation barriers and reaction thermodynamic parameters, as well as kinetic and equilibrium constants for the deprotonation have been computed at  $T = 10, 50, 150, 200$  and  $300\text{ K}$ . It resulted that at the temperatures typical of dark clouds (10 K) the majority of HCN–forsterite complexes results in the deprotonation of the molecule. At the conditions proper of outer proto-planetary disks (50–150 K) and of small celestial bodies ( $T = 200$ – $300\text{ K}$ ) this tendency is even enhanced, an important implication for HCN reactivity, which is considered a fundamental outcome of the present research. Ongoing work is devoted to study the HCN polymerization towards adenine.

Finally, a spectroscopic vibrational analysis has been performed, focusing on the stretching frequencies of the C–H,  $\text{C}\equiv\text{N}$  and O–H bonds. Good correlations have been observed between the bond lengths and the corresponding stretching frequencies, hence providing a way to determine the degree of perturbation of the C–H and  $\text{C}\equiv\text{N}$  bonds of HCN upon adsorption, which is an indicator for the subsequent polymerization. In particular, the  $\text{C}\equiv\text{N}$  frequencies undergo both bathochromic and hypsochromic shifts due to adsorption, depending on the type and number of simultaneous





interactions occurring with surface  $\text{Mg}^{2+}$  cations and the strength of the H-bonds formed. More specifically, it was observed that  $\text{Mg-N}$ ,  $\text{NC}^{\cdots}\text{HO-Si}$ , and lateral  $\text{Mg-C}\equiv\text{N}$  interactions contribute to bathochromic shifts of the  $\text{C}\equiv\text{N}$  bonds, while bridged  $\text{Mg-CN-Mg}$  motifs cause hypsochromic shifts.

## Conflicts of interest

There are no conflicts to declare.

## Acknowledgements

This project has received funding within the European Union's Horizon 2020 research and innovation program from the European Research Council (ERC) for the project "Quantum Chemistry on Interstellar Grains" (Quantumgrain), grant agreement No. 865657, and from the Marie Skłodowska-Curie for the project "Astro-Chemical Origins" (ACO), grant agreement No. 811312. The Italian Space Agency for co-funding the Life in Space Project (ASI N. 2019-3-U.O.), the Italian MUR (PRIN 2020, Astrochemistry beyond the second period elements, Prot. 2020AFB3FX) are also acknowledged for financial support. This research is also funded by MICINN (project PID2021-126427NB-I00). This research acknowledges support from the Project CH4.0 under the MIUR program "Dipartimento di Eccellenza 2023-2027".

## References

- 1 A. M. S. Boonman, R. Stark, F. F. S. van der Tak, E. F. van Dishoeck, P. B. van der Wal, F. Schafer, G. de Lange and W. M. Laauwen, Highly abundant HCN in the inner hot envelope of GL 2591: probing the birth of a hot core?, *Astrophys. J.*, 2001, **553**, L63–L67.
- 2 H.-C. Huang, Y.-J. Kuan, S. B. Charnley, N. Hirano, S. Takakuwa and T. L. Bourke, Organic molecules in the hot corinos and circumstellar disks of IRAS 16293-2422, *Adv. Space Res.*, 2005, **36**, 146–155.
- 3 T. S. Rice, E. A. Bergin, J. K. Jørgensen and S. F. Wampfler, Exploring the origins of Earth's nitrogen: Astronomical observations of nitrogen-bearing organics in protostellar environments, *Astrophys. J.*, 2018, **866**, 156.
- 4 M. N. Drozdovskaya, E. F. van Dishoeck, M. Rubin, J. K. Jørgensen and K. Altwegg, Ingredients for solar-like systems: protostar IRAS 16293-2422 B versus comet 67P/Churyumov-Gerasimenko, *Mon. Not. R. Astron. Soc.*, 2019, **490**, 50–79.
- 5 A. Dutrey, S. Guilloteau and M. Guelin, Chemistry of protosolar-like nebulae: The molecular content of the DM Tau and GG Tau disks, *Astron. Astrophys.*, 1997, **317**, L55–L58.
- 6 W.-F. Thi, G.-J. van Zadelhoff and E. F. van Dishoeck, Organic molecules in protoplanetary disks around T Tauri and Herbig Ae stars, *Astron. Astrophys.*, 2004, **425**, 955–972.
- 7 J. B. Bergner, K. I. Öberg, E. A. Bergin, R. A. Loomis, J. Pegues and C. Qi, A Survey of  $\text{C}_2\text{H}$ , HCN, and  $\text{C}_{18}\text{O}$  in Protoplanetary Disks, *Astrophys. J.*, 2019, **876**, 25.
- 8 V. V. Guzmán, J. B. Bergner, C. J. Law, K. I. Öberg, C. Walsh, G. Cataldi, Y. Aikawa, E. A. Bergin, I. Czekala, J. Huang, S. M. Andrews, R. A. Loomis, K. Zhang, R. Le Gal, F. Alarcón, J. D. Ilee, R. Teague, L. I. Cleaves, D. J. Wilner, F. Long, K. R. Schwarz, A. D. Bosman, L. M. Pérez, F. Ménard and Y. Liu, Molecules with ALMA at Planet-forming Scales (MAPS). VI. Distribution of the Small Organics HCN,  $\text{C}_2\text{H}$ , and  $\text{H}_2\text{CO}$ , *Astrophys. J., Suppl. Ser.*, 2021, **257**, 6.
- 9 E. S. Wirstrom, M. S. Lerner, P. Källström, A. Levinsson, A. Olivefors and E. Teggehall, HCN observations of comets C/2013 R1 (Lovejoy) and C/2014 Q2 (Lovejoy), *Astron. Astrophys.*, 2016, **588**, A72.
- 10 W. F. Huebner, L. E. Snyder and D. Buhl, HCN radio emission from Comet Kohoutek (1973f), *Icarus*, 1974, **23**, 580–584.
- 11 S. Pizzarello, Hydrogen Cyanide in the Murchison Meteorite, *Astrophys. J.*, 2012, **754**, L27.
- 12 L. Tanguy, B. Bézard, A. Marten, D. Gautier, E. Gérard, G. Paubert and A. Lecacheux, Stratospheric profile of HCN on Titan from millimeter observations, *Icarus*, 1990, **85**, 43–57.
- 13 M. Rengel, D. Shulyak, P. Hartogh, H. Sagawa, R. Moreno, C. Jarchow and D. Breitschwerdt, Ground-based HCN sub-millimetre measurements in Titan's atmosphere: an inter-comparison with Herschel observations, *Astron. Astrophys.*, 2022, **658**, A88.
- 14 R. J. de Kok, N. A. Teanby, L. Maltagliati, P. G. J. Irwin and S. Vinatier, HCN ice in Titan's high-altitude southern polar cloud, *Nature*, 2014, **514**, 65–67.
- 15 H. Liszt and R. Lucas, Comparative chemistry of diffuse clouds - II. CN, HCN, HNC,  $\text{CH}_3\text{CN}$  &  $\text{N}_2\text{H}^+$ , *Astron. Astrophys.*, 2001, **370**, 576–585.
- 16 T. Hirota, S. Yamamoto, H. Mikami and M. Ohishi, Abundances of HCN and HNC in Dark Cloud Cores, *Astrophys. J.*, 1998, **503**, 717–728.
- 17 J. Oró, Mechanism of Synthesis of Adenine from Hydrogen Cyanide under Possible Primitive Earth Conditions, *Nature*, 1961, **191**, 1193–1194.
- 18 Z. Martins, O. Botta, M. L. Fogel, M. A. Sephton, D. P. Glavin, J. S. Watson, J. P. Dworkin, A. W. Schwartz and P. Ehrenfreund, Extraterrestrial Nucleobases in the Murchison Meteorite, *Origins Life Evol. Biospheres*, 2009, **30**, 214.
- 19 C. N. Matthews and R. Ludicky, *ESLAB Symposium on the Exploration of Halley's Comet*, 1986, vol. **250**.
- 20 D. P. Cruikshank, L. J. Allamandola, W. K. Hartmann, D. J. Tholen, R. H. Brown, C. N. Matthews and J. F. Bell, Solid  $\text{C}\equiv\text{N}$  bearing material on outer solar system bodies, *Icarus*, 1991, **94**, 345–353.
- 21 C. N. Matthews, Heteropolypeptides on Titan?, *Origins Life*, 1982, **12**, 281–283.
- 22 C. N. Matthews, Hydrogen cyanide polymers: from laboratory to space, *Planet. Space Sci.*, 1995, **43**, 1365–1370.
- 23 R. A. Sanchez, J. P. Ferbis and L. E. Orgel, Studies in Prebiotic Synthesis: II. Synthesis of purine precursors and



- amino acids from aqueous hydrogen cyanide, *J. Mol. Biol.*, 1967, **30**, 223–253.
- 24 M. K. Yim and J. C. Choe, Dimerization of HCN in the gas phase: a theoretical mechanistic study, *Chem. Phys. Lett.*, 2012, **538**, 24–28.
  - 25 S. H. Jung and J. C. Choe, Mechanisms of prebiotic adenine synthesis from HCN by oligomerization in the gas phase, *Astrobiology*, 2013, **13**, 465–475.
  - 26 B. Fábíán, M. Szőri and P. Jedlovský, Floating Patches of HCN at the Surface of Their Aqueous Solutions – Can They Make “HCN World” Plausible?, *J. Phys. Chem. C*, 2014, **118**, 21469–21482.
  - 27 H. Sandstrom and M. Rahm, The Beginning of HCN Polymerization: Iminoacetonitrile Formation and Its Implications in Astrochemical Environments, *ACS Earth Space Chem.*, 2021, **5**, 2152–2159.
  - 28 J. C. Choe, Water-assisted Dimerization of Hydrogen Cyanide: A Computational Study, *Bull. Korean Chem. Soc.*, 2017, **38**, 1531–1533.
  - 29 O. Kikuchi, T. Watanabe, Y. Satoh and Y. Inadomi, Ab initio GB study of prebiotic synthesis of purine precursors from aqueous hydrogen cyanide: dimerization reaction of HCN in aqueous solution, *THEOCHEM*, 2000, **507**, 53–62.
  - 30 I. W. M. Smith, D. Talbi and E. Herbst, The production of HCN dimer and more complex oligomers in dense interstellar clouds, *Astron. Astrophys.*, 2001, **369**, 611–615.
  - 31 R. Santalucia, M. Pazzi, F. Bonino, M. Signorile, D. Scarano, P. Ugliengo, G. Spoto and L. Mino, From gaseous HCN to nucleobases at the cosmic silicate dust surface: an experimental insight into the onset of prebiotic chemistry in space, *Phys. Chem. Chem. Phys.*, 2022, **24**, 7224–7230.
  - 32 J. C. Choe, Dimerization of HCN in Interstellar Icy Grain Mantles: A DFT Study, *Bull. Korean Chem. Soc.*, 2019, **40**, 205–206.
  - 33 M. Signorile, L. Zamirri, A. Tsuchiyama, P. Ugliengo, F. Bonino and G. Martra, On the Surface Acid–Base Properties of Amorphous and Crystalline  $\text{Mg}_2\text{SiO}_4$  as Probed by Adsorbed  $\text{CO}$ ,  $\text{CO}_2$ , and  $\text{CD}_3\text{CN}$ , *ACS Earth Space Chem.*, 2020, **4**, 345–354.
  - 34 T. Henning, Cosmic Silicates, *Annu. Rev. Astron. Astrophys.*, 2010, **48**, 21–46.
  - 35 P. R. Buseck and H. Xin Hua, Matrices of carbonaceous chondrite meteorites, *Annu. Rev. Earth Planet. Sci.*, 1993, **21**, 255–305.
  - 36 A. H. Delsemme, S. K. Runcorn, G. Turner and M. M. Woolfson, The chemistry of comets, *Philos. Trans. R. Soc., A*, 1988, **325**, 509–523.
  - 37 A. M. Walker, S. M. Woodley, B. Slater and K. Wright, A computational study of magnesium point defects and diffusion in forsterite, *Phys. Earth Planet. Inter.*, 2009, **172**, 20–27.
  - 38 G. Ottonello, B. Civalieri, J. Ganguly, M. Vetuschi Zuccolini and Y. Noel, Thermophysical properties of the  $\alpha$ – $\beta$ – $\gamma$  polymorphs of  $\text{Mg}_2\text{SiO}_4$ : a computational study, *Phys. Chem. Miner.*, 2009, **36**, 87–106.
  - 39 J. Navarro-Ruiz, P. Ugliengo, A. Rimola and M. Sodupe, B3LYP Periodic Study of the Physicochemical Properties of the Nonpolar (010) Mg-Pure and Fe-Containing Olivine Surfaces, *J. Phys. Chem. A*, 2014, **118**, 5866–5875.
  - 40 M. Bruno, F. R. Massaro, M. Prencipe, R. Demichelis, M. De La Pierre and F. Nestola, Ab initio calculations of the main crystal surfaces of forsterite ( $\text{Mg}_2\text{SiO}_4$ ): a preliminary study to understand the nature of geochemical processes at the olivine interface, *J. Phys. Chem. C*, 2014, **118**, 2498–2506.
  - 41 R. Demichelis, M. Bruno, F. R. Massaro, M. Prencipe, M. De La Pierre and F. Nestola, First-principle modelling of forsterite surface properties: Accuracy of methods and basis sets, *J. Comput. Chem.*, 2015, **36**, 1439–1445.
  - 42 J. Navarro-Ruiz, M. Sodupe, P. Ugliengo and A. Rimola, Interstellar H adsorption and  $\text{H}_2$  formation on the crystal-line (010) forsterite surface: a B3LYP-D2\* periodic study, *Phys. Chem. Chem. Phys.*, 2014, **16**, 17447–17457.
  - 43 J. Navarro-Ruiz, J. Á. Martínez-González, M. Sodupe, P. Ugliengo and A. Rimola, Relevance of silicate surface morphology in interstellar  $\text{H}_2$  formation. Insights from quantum chemical calculations, *Mon. Not. R. Astron. Soc.*, 2015, **453**, 914–924.
  - 44 S. Garcia-Gil, D. Teillet-Billy, N. Rougeau and V. Sidis, H Atom Adsorption on a Silicate Surface: The (010) Surface of Forsterite, *J. Phys. Chem. C*, 2013, **117**, 12612–12621.
  - 45 T. Suhasaria, J. D. Thrower and H. Zacharias, Thermal desorption of astrophysically relevant molecules from forsterite(010), *Mon. Not. R. Astron. Soc.*, 2017, **472**, 389–399.
  - 46 G. Molpeceres, A. Rimola, C. Ceccarelli, J. Kästner, P. Ugliengo and B. Maté, Silicate-mediated interstellar water formation: a theoretical study, *Mon. Not. R. Astron. Soc.*, 2019, **482**, 5389–5400.
  - 47 T. Liu, S. S. Gautam, L. L. Daemen, A. I. Kolesnikov, L. M. Anovitz, M. Hartl and D. R. Cole, Vibrational Behavior of Water Adsorbed on Forsterite ( $\text{Mg}_2\text{SiO}_4$ ) Surfaces, *ACS Earth Space Chem.*, 2020, **4**, 1050–1063.
  - 48 R. S. Smith, Z. Li, Z. Dohnálek and B. D. Kay, Adsorption, Desorption, and Displacement Kinetics of  $\text{H}_2\text{O}$  and  $\text{CO}_2$  on Forsterite,  $\text{Mg}_2\text{SiO}_4(011)$ , *J. Phys. Chem. C*, 2014, **118**, 29091–29100.
  - 49 H. E. King, M. Stimpfl, P. Deymier, M. J. Drake, C. R. A. Catlow, A. Putnis and N. H. de Leeuw, Computer simulations of water interactions with low-coordinated forsterite surface sites: Implications for the origin of water in the inner solar system, *Earth Planet. Sci. Lett.*, 2010, **300**, 11–18.
  - 50 T. P. M. Goumans, C. R. A. Catlow, W. A. Brown, J. Kästner and P. Sherwood, An embedded cluster study of the formation of water on interstellar dust grains, *Phys. Chem. Chem. Phys.*, 2009, **11**, 5431–5436.
  - 51 N. H. de Leeuw, S. C. Parker, C. R. A. Catlow and G. D. Price, Modelling the effect of water on the surface structure and stability of forsterite, *Phys. Chem. Miner.*, 2000, **27**, 332–341.
  - 52 K. Muralidharan, P. Deymier, M. Stimpfl, N. H. de Leeuw and M. J. Drake, Origin of water in the inner Solar System: A kinetic Monte Carlo study of water adsorption on forsterite, *Icarus*, 2008, **198**, 400–407.
  - 53 L. Zamirri, M. Corno, A. Rimola and P. Ugliengo, Forsterite Surfaces as Models of Interstellar Core Dust Grains:



- Computational Study of Carbon Monoxide Adsorption, *ACS Earth Space Chem.*, 2017, **1**, 384–398.
- 54 L. Zamirri, S. Pantaleone and P. Ugliengo, Carbon monoxide adsorption at forsterite surfaces as models of interstellar dust grains: An unexpected bathochromic (red) shift of the CO stretching frequency, *J. Chem. Phys.*, 2019, **150**, 064702.
  - 55 A. Rimola, J. M. Trigo-Rodríguez and Z. Martins, Interaction of organic compounds with chondritic silicate surfaces. Atomistic insights from quantum chemical periodic simulations, *Phys. Chem. Chem. Phys.*, 2017, **19**, 18217–18231.
  - 56 A. M. Asaduzzaman, T. J. Zega, S. Laref, K. Runge, P. A. Deymier and K. Muralidharan, A computational investigation of adsorption of organics on mineral surfaces: Implications for organics delivery in the early solar system, *Earth Planet. Sci. Lett.*, 2014, **408**, 355–361.
  - 57 E. Escamilla-Roa and C. I. Sainz-Díaz, Amorphous Ammonia–Water Ice Deposited onto Silicate Grain: Effect on Growth of Mantles Ice on Interstellar and Interplanetary Dust, *J. Phys. Chem. C*, 2014, **118**, 3554–3563.
  - 58 T. Suhasaria, J. D. Thrower and H. Zacharias, Thermal desorption of ammonia from crystalline forsterite surfaces, *Mon. Not. R. Astron. Soc.*, 2015, **454**, 3317–3327.
  - 59 M. A. Corazzi, D. Fedele, G. Poggiali and J. R. Brucato, Photoprocessing of formamide ice: route towards prebiotic chemistry in space, *Astron. Astrophys.*, 2020, **636**, A63.
  - 60 E. Escamilla-Roa and F. Moreno, Adsorption of glycine by cometary dust: Astrobiological implications, *Planet. Space Sci.*, 2012, **70**, 1–9.
  - 61 E. Escamilla-Roa and F. Moreno, Adsorption of glycine on cometary dust grains: II—Effect of amorphous water ice, *Planet. Space Sci.*, 2013, **75**, 1–10.
  - 62 E. Escamilla-Roa and C. I. Sainz-Díaz, Effect of Amorphous Ammonia–Water Ice onto Adsorption of Glycine on Cometary Dust Grain and IR Spectroscopy, *J. Phys. Chem. C*, 2014, **118**, 26080–26090.
  - 63 A. Li and B. T. Draine, On ultrasmall silicate grains in the diffuse interstellar medium, *Astrophys. J.*, 2001, **550**, L213.
  - 64 R. Dovesi, A. Erba, R. Orlando, C. M. Zicovich-Wilson, B. Civalleri, L. Maschio, M. Rérat, S. Casassa, J. Baima and S. Salustro, Quantum-mechanical condensed matter simulations with CRYSTAL, *Wiley Interdiscip. Rev.: Comput. Mol. Sci.*, 2018, **8**, e1360.
  - 65 J. P. Perdew, K. Burke and M. Ernzerhof, Generalized gradient approximation made simple, *Phys. Rev. Lett.*, 1996, **77**, 3865.
  - 66 S. Grimme, Semiempirical GGA-type density functional constructed with a long-range dispersion correction, *J. Comput. Chem.*, 2006, **27**, 1787–1799.
  - 67 M. Cutini, L. Maschio and P. Ugliengo, Exfoliation energy of layered materials by DFT-D: Beware of dispersion!, *J. Chem. Theory Comput.*, 2020, **16**, 5244–5252.
  - 68 B. Civalleri, C. M. Zicovich-Wilson, L. Valenzano and P. Ugliengo, B3LYP augmented with an empirical dispersion term (B3LYP-D\*) as applied to molecular crystals, *CrystEngComm*, 2008, **10**, 405–410.
  - 69 A. Schäfer, H. Horn and R. Ahlrichs, Fully optimized contracted Gaussian basis sets for atoms Li to Kr, *J. Chem. Phys.*, 1992, **97**, 2571–2577.
  - 70 C. G. Broyden, The Convergence of a Class of Double-rank Minimization Algorithms 1. General Considerations, *IMA J. Appl. Math.*, 1970, **6**, 76–90.
  - 71 R. Fletcher, A new approach to variable metric algorithms, *Comput. J.*, 1970, **13**, 317–322.
  - 72 D. Goldfarb, A family of variable-metric methods derived by variational means, *Math. Comput.*, 1970, **24**, 23–26.
  - 73 D. F. Shanno, Conditioning of quasi-Newton methods for function minimization, *Math. Comput.*, 1970, **24**, 647–656.
  - 74 M. Corno and P. Ugliengo, Surface modeling of ceramic biomaterials, in *Encyclopedia of Nanotechnology*, ed. B. Bhushan, Springer Science + Business Media, 2015, pp. 1–13.
  - 75 H. B. Jansen and P. Ros, Non-empirical molecular orbital calculations on the protonation of carbon monoxide, *Chem. Phys. Lett.*, 1969, **3**, 140–143.
  - 76 B. Liu and A. D. McLean, Accurate calculation of the attractive interaction of two ground state helium atoms, *J. Chem. Phys.*, 1973, **59**, 4557–4558.
  - 77 S. F. Boys and F. Bernardi, The calculation of small molecular interactions by the differences of separate total energies. Some procedures with reduced errors, *Mol. Phys.*, 1970, **19**, 553–566.
  - 78 D. A. Williams, The interstellar medium: an overview, *Solid State Astrochem.*, 2003, 1–20.
  - 79 K. Nakamoto, *Handbook of Vibrational Spectroscopy*, John Wiley & Sons, Ltd, 2006.
  - 80 C. M. Zicovich-Wilson, M. L. San Román and A. Ramírez-Solís, Mechanism of F- elimination from zeolitic D4R units: A periodic B3LYP study on the octadecasil zeolite, *J. Phys. Chem. C*, 2010, **114**, 2989–2995.
  - 81 R. A. Marcus and O. K. Rice, The Kinetics of the Recombination of Methyl Radicals and Iodine Atoms, *J. Phys. Chem.*, 1951, **55**, 894–908.
  - 82 R. A. Marcus, Unimolecular Dissociations and Free Radical Recombination Reactions, *J. Chem. Phys.*, 1952, **20**, 359–364.
  - 83 H. M. Rosenstock, M. B. Wallenstein, A. L. Wahrhaftig and H. Eyring, Absolute Rate Theory for Isolated Systems and the Mass Spectra of Polyatomic Molecules, *Proc. Natl. Acad. Sci. U. S. A.*, 1952, **38**, 667–678.
  - 84 T. Baer and W. L. Hase, *Unimolecular Reaction Dynamics: Theory and Experiments*, Oxford University Press, USA, 1996.
  - 85 C. Eckart, The penetration of a potential barrier by electrons, *Phys. Rev.*, 1930, **35**, 1303.
  - 86 H. S. Johnston and J. Heicklen, Tunnelling corrections for unsymmetrical Eckart potential energy barriers, *J. Phys. Chem.*, 1962, **66**, 532–533.
  - 87 J. R. Smyth and R. M. Hazen, The crystal structures of forsterite and hortonolite at several temperatures up to 900 C, *Am. Mineral. J. Earth Planet. Mater.*, 1973, **58**, 588–593.
  - 88 G. W. Watson, P. M. Oliver and S. C. Parker, Computer simulation of the structure and stability of forsterite surfaces, *Phys. Chem. Miner.*, 1997, **25**, 70–78.



- 89 D. Bostrom, Single-crystal X-ray diffraction studies of synthetic Ni-Mg olivine solid solutions, *Am. Mineral.*, 1987, **72**, 965–972.
- 90 M. De La Pierre, R. Orlando, L. Maschio, K. Doll, P. Ugliengo and R. Dovesi, Performance of six functionals (LDA, PBE, PBESOL, B3LYP, PBE0, and WC1LYP) in the simulation of vibrational and dielectric properties of crystalline compounds. The case of forsterite  $\text{Mg}_2\text{SiO}_4$ , *J. Comput. Chem.*, 2011, **32**, 1775–1784.
- 91 P. W. Tasker, The stability of ionic crystal surfaces, *J. Phys. C-Solid State Phys.*, 1979, **12**, 4977.
- 92 G. Wulff, Xxv. zur frage der geschwindigkeit des wachstums und der auflösung der krystallflächen, *Z. Kristallogr. - Cryst. Mater.*, 1901, **34**, 449–530.
- 93 A. Natta, L. Testi, N. Calvet, T. Henning, R. Waters and D. Wilner, in *Protostars and Planets V*, ed. D. Jewitt and K. Keil, University of Arizona Press, Tucson, 2007, pp. 767–781.
- 94 L. Zamirri, A. Macià Escatllar, J. Mariñoso Guiu, P. Ugliengo and S. T. Bromley, What Can Infrared Spectra Tell Us about the Crystallinity of Nanosized Interstellar Silicate Dust Grains?, *ACS Earth Space Chem.*, 2019, **3**, 2323–2338.
- 95 G. Pacchioni, G. Cogliandro and P. S. Bagus, Characterization of oxide surfaces by infrared spectroscopy of adsorbed carbon monoxide: a theoretical investigation of the frequency shift of CO on MgO and NiO, *Surf. Sci.*, 1991, **255**, 344–354.
- 96 G. Pacchioni, A. M. Ferrari and P. S. Bagus, Cluster and band structure ab initio calculations on the adsorption of CO on acid sites of the  $\text{TiO}_2$  (110) surface, *Surf. Sci.*, 1996, **350**, 159–175.
- 97 L. Mino, A. M. Ferrari, V. Lacivita, G. Spoto, S. Bordiga and A. Zecchina, CO Adsorption on Anatase Nanocrystals: A Combined Experimental and Periodic DFT Study, *J. Phys. Chem. C*, 2011, **115**, 7694–7700.

